Mechanistic foam flow model with variable flowing foam fraction and its implementation using automatic differentiation

Muhammad M. Almajid [a,b], Zhi Yang Wong [b], Anthony R. Kovscek [b,*]

[a] EXPEC Advanced Research Center, Dhahran, Saudi Arabia
[b] Energy Resources Engineering, 367 Panama St., Room 050, Stanford, CA 94305, USA

ARTICLE INFO

ABSTRACT

Foam injection is an effective method for modifying gas mobility in subsurface flow applications making it ideal for environmental remediation applications. Remediation of contaminated soils/aquifers of nonaqueous phase liquids using foamed surfactant solutions is a viable option but a predictive foam model is needed that is flexible to the addition of more accurate physical descriptions. Such a model is essential to ensure successful operations in soil remediation applications. The objective of this paper is to develop a full-physics, mechanistic transient foam flow model and integrate it into the multiphysics, modular AD-GPRS framework (Automatic Differentiation–General Purpose Research Simulator). We chose AD-GPRS because it allows rapid prototyping and addition of complex physics and modeling strategies. We develop the model ground-up from pore-scale observations and implement a new flowing foam fraction constitutive relation that depends on the local pressure gradient, local permeability, and flowing bubble density. Our model predicts the two flow regimes commonly observed in steady-state pressure gradient measurements: the low-quality regime and the high-quality regime. Additionally, the model is used to match transient experimental results of homogeneous and slightly heterogeneous cores with a wide range of permeability values. The implementation of this model within AD-GPRS allows testing of ideas and modeling strategies as well as inclusion of more complex physics or foam generation kinetics.

1. Introduction

Subsurface aquifer/soil contaminant remediation is a complicated process due to complexities introduced by fluid/fluid interactions, fluid/rock interactions, or rock heterogeneities. The contaminants could exist as free phase in the pore space of soils and/or bind tightly on the soil/rock surfaces (Wang and Mulligan, 2004). The density of some nonaqueous phase liquids (NAPLs) is larger than the resident water. Hence, they migrate through the vadose zone to the bottom of the aquifer where permeability is small, and often become immobilized (Hirasaki et al., 1997a). Additionally, the insolubility and/or immiscibility of these NAPLs in water and the large interfacial tension between them and water makes traditional remediation efforts such as pump-and-treat difficult (Oolman et al., 1995; Pope and Wade, 1995; Hirasaki et al., 1997a; Wang and Mulligan, 2004).

An effective method that has the potential to alleviate some of the challenges faced during remediation processes is to foam an injection gas. Foams also are relevant to the storage of carbon dioxide in saline formations (Eide et al., 2020). The discontinuity of the gaseous phase in foams gives them the advantage to make remediation efforts more effective. Because bubbles are separated by thin liquid films, foams develop a much larger apparent viscosity when compared to gas alone (Hirasaki and Lawson, 1985). Moreover, the discontinuity of the gaseous phase helps foams to immobilize, or trap, more gas in the high-permeability layers (Tang and Kovscek, 2006) that ultimately diverts some of the gas to the lower-permeability layers. Therefore, foams can enhance the sweep of aqueous surfactant solutions by diverting injectants to low-permeability zones during aquifer/soil remediation jobs. Diversion ultimately aids greater drainage of contaminants out of the affected zones (Hirasaki et al., 1997b).

Hirasaki et al. (1997b) demonstrated that foam is successful for environmental aquifer restoration purposes. An aquifer that had been contaminated with dense NAPL was chosen to examine the effectiveness of using foamed surfactant solution to clean the NAPL from the aquifer. The chosen aquifer was characterized as heterogeneous because it contained thief zones that had permeability upwards of 100 Darcy and relatively tighter zones that had permeabilities that were 40 Darcy or smaller. The NAPL was trapped primarily in the tighter zones towards the bottom of the aquifer and, therefore, presented an additional challenge for other remediation processes such as pump-and-treat, or surfactant-based remediation processes, that are incapable of diverting liquids to the lower-permeability zones (Hirasaki et al., 1997a). Foam removed essentially

---

all of the NAPL from the swept pore volume as evidenced by tracer tests that measured a reduced average NAPL saturation of only 0.03% (Hirasaki et al., 1997a; Szafranski et al., 1998).

There were key observations and important lessons learned from the demonstration project. First, air injection pressure to produce foam was low and the pressure gradient necessary for foam propagation was kept small. Second, foam diverted the surfactant solution from high-permeability zones to the low-permeability zones. This implies that trapped foam behaved differently in thief zones than in tight zones. Moreover, it seems that as foam flowed initially into the thief zones, it built a relatively larger pressure gradient and, hence, the trapped foam fraction was large. The trapped foam fraction is the fraction of the gas saturation that is immobile, in a time-averaged sense. On the other hand, lower-permeability zones received diverted foam that was described as "frothy" indicating that the trapped foam fraction was less when pressure gradients were small. Mamun et al. (2002) confirmed that the two flow regimes commonly observed in petroleum applications (i.e. low-quality and high-quality regimes) also apply in this low-pressure-gradient that is applicable to environmental remediation. In related work, Tang and Kovscek (2006) performed an extensive study of the variables influencing the trapped foam fraction in porous media and reported that the portion of the foam that flows differs with pressure gradient, permeability, and bubble density. Moreover, pore network analysis shows that trapped foam varies with bubble density and pressure gradient (Kharabaf and Yortsos, 1998; Almajid and Kovscek, 2019).

We anticipate that in low-pressure-gradient environments such as those encountered during environmental remediation that the trapped foam fraction is sensitive to the evolved pressure gradient due to foam. Therefore, an improved foam flow model that takes this effect into account is needed for more accurate predictive modeling of foam remediation processes. Additionally, a framework that allows easy and rapid prototyping of improved physical descriptions that is capable of interweaving upscaled pore-scale phenomena is needed. The framework should be extensible to multidimensions such that predictive models are readily extended to aquifer scale (10's of meter scale). Because it is a significant undertaking to move to aquifer scale directly, this paper focuses attention on the meter scale (core scale) where we develop and verify a mechanistic population balance model that is built on physical pore scale observations. While the destabilizing mechanisms of foam in the presence of NAPL are important, this paper takes a first step and develops a model that works in the absence of NAPL or at residual saturation of NAPLs.

Accordingly, the objective of this paper is to develop and implement a transient foam model that is based on physical observations and is capable of predicting foam transport behavior in porous media. There are several approaches to model foam flow. Empirical, local-equilibrium, or full-physics models have been used in the past (Ma et al., 2015). We seek a framework that is easy to manipulate to include more complex physics to describe foam flow. To that end, we use the modular, multiphysics framework of the Automatic Differentiation General Purpose Research Simulator AD-GPRS and add a foam simulation option. The mechanistic population balance model developed is compared to data from new transient foam flooding experiments. Homogeneous foam flow experimental data in the case of constant and transient surfactant were used to validate the simulator predictions (Kovscek et al., 1995). Importantly, heterogeneous low- and high-quality transient foam flow experiments were conducted and matched to a reasonable degree of accuracy.

The model developed differs from current foam models and especially from that of Chen et al. (2010) in three ways. First, our numerical implementation uses the automatic differentiation capability of AD-GPRS to compute the Jacobian thereby permitting more rapid prototyping of equations. Second, the foam model used in Chen et al. (2010) is a local equilibrium foam model. Their model assumes instantaneous equilibrium between generation and coalescence as soon as gas and enough surfactant are present in the same grid block. Based on this instanta-
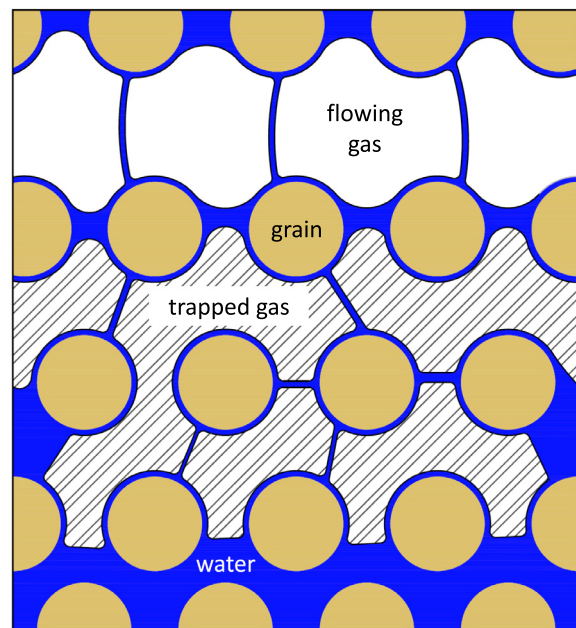

Fig. 1. Time-averaged schematic of foam in porous media. The beige-colored grains are made small and the porosity large to emphasize pore-scale details of bubble arrangement. Dispersed gas bubbles separated by surfactant-stabilized thin films flow in the largest and least resistive pore space. Trapped gas bubbles are found in intermediate-sized pores. By volume, the majority of the dispersed gas phase is trapped. Water fills completely the smallest pore space with the greatest capillary entry pressure.

neous equilibrium, the bubble density is computed algebraically. Therefore, the bubble density is not a primary variable that is solved for numerically. Our current work does not assume local equilibrium. Hence, we solve the full-physics model and include the bubble density as a primary variable along with pressure and water saturation as outlined in later sections. Third, the flowing foam fraction (X_f) used in the work of Chen et al. (2010) is based only on the bubble density. In the current work, however, X_f depends on the pressure gradient, permeability, and bubble density.

This paper proceeds by presenting a pore-scale depiction of how foam resides in the pore space. A quick overview of the experimental set-up and procedures is outlined next. Then, the theoretical foundation of the mechanistic population balance model is presented. Model predictions of experimental cases are presented next. Finally, we lay out a concise summary of this paper's findings.

2. Foam in porous media

Foam in porous media is defined as a dispersion of gas in a continuous liquid phase. Fig. 1 illustrates a pore-level description of foam (Ettinger and Radke, 1992; Gillis and Radke, 1990; Chambers and Radke, 1991; Kovscek and Radke, 1994). In the figure, the grains are indicated by the beige-colored circles, flowing gas by clear white shading, trapped gas by the hatched white shading, and the wetting-aqueous phase by blue coloring. For better illustration of the distribution of fluids, the highly schematic figure has three pore spaces of increasing dimension. The pore space increases in size from the lower part of the figure moving upwards.

In accordance with capillarity, the wetting-aqueous phase fills the smallest pore space and attaches to the grains by thin liquid films. Note, the liquid phase is continuous. Therefore, the liquid relative permeability in the presence of foam remains unchanged because only small amounts of liquid travel in the thin, surfactant-stabilized films, called lamellae, that subdivide the gas phase. During transient foam flow,

lamellae resist flow and, hence, bubble trains favor flowing in the least resistive pathways (Almajid and Kovscek, 2019). The flowing bubbles convect convec through the largest-sized pore space while trapped bubbles block gas flow through the intermediate-sized pore space.

In the presence of strong foam, gas mobility is modified by a combination of an increase in the gas apparent viscosity and an increase in the trapped gas fraction. Because of the drag that flowing bubbles experience due to the pore walls and pore constrictions (Falls et al., 1989) and the constant rearrangement of the gas-liquid interfacial area of flowing bubbles due to viscous and capillary forces (Hirasaki and Lawson, 1985), the viscosity of the foamed-gas appears much larger than that of unfoamed-gas. Significantly, gas tracer experiments (Gillis and Radke, 1990; Friedmann et al., 1991; Tang and Kovscek, 2006) infer fractions of trapped gas from effluent data that range from 85% to 99% depending on the flow conditions. Moreover, direct X-ray computed tomography (CT) estimates in-situ trapped gas fractions between 36% and 70% and shows how the tracer concentration is not uniform along the length of the core (Nguyen et al., 2009).

Lamellae that separate the flowing and trapped gas bubbles evolve from a balance between generation and coalescence mechanisms that depend on the flow conditions as well as the initial and boundary conditions of the porous medium. Additionally, generation and coalescence mechanisms set the final distribution of the bubbles in the porous medium (Ettinger and Radke, 1992; Almajid et al., 2019). Several microvisual studies confirmed that lamellae are generated by one of three generation mechanisms: snap-off, lamellae division, or leave-behind (Chambers and Radke, 1991; Almajid and Kovscek, 2016). In the absence of oil, coalescence is mainly dominated by the capillary suction mechanism. Gas diffusion between neighboring bubbles could also destroy the generated lamellae but its effect is minimal in comparison to the capillary suction mechanism. The details of these generation and coalescence mechanisms are laid out elsewhere (Almajid and Kovscek, 2016).

3. Experimental set-up and procedures

Foam flow experiments were performed using a heterogeneous sandstone core. The core was placed inside an aluminum core holder that allows the acquisition of images necessary to track the water saturation during the experiments. Fig. 2 shows a schematic of the experimental set up. The core was chosen such that its length (60 cm) is much greater than the entry length for net foam generation (~12 cm) (Chen, 2009). Fig. 3a shows a reconstructed porosity image of the core we used. The average porosity of the core was about 25%, Fig. 3b, but there were tighter laminations cutting through it at an angle that made it slightly heterogeneous, Fig. 3a.

Pressure and water saturation profiles were tracked during the experiments. Aqueous-phase saturation was obtained using an X-ray CT scanner. The experimental set up and procedures are identical to those outlined elsewhere and the reader is encouraged to consult these citations for more details about the experiments (Almajid, 2019; Almajid et al., 2019).

During a transient foam flow experiment, the vacuumed clean core is initially flushed with CO_2 and then fully-saturated with 0.5 wt% NaCl brine. Backpressure is released and reapplied periodically to assist in removing all gas from the system. The brine is then replaced with a foamer solution. The foamer solution contains 0.5 wt% active Stepan Bioterg AS40 (sodium C14-16 olefin sulfonate) in 0.5 wt% NaCl brine. The gas and the foamer solution are coinjected into the core that is at a prespecified backpressure ($\approx$ 100 psi). The injected density of bubbles is, therefore, zero because no foam pregenerator is used.

Gas injection is achieved with a mass flow controller (Brooks Mass Flow Controller 5850TR) while liquid injection is controlled by a dual-piston Quizix pump (Quizix QX5000). Gas Darcy velocities range from 0.14 m/day to 1.90 m/day at the prescribed backpressure while liquid Darcy velocities range from 0.14 m/day to 0.21 m/day.

4. Model development

4.1. Governing equations

Mass conservation equations for the gaseous and aqueous phases are the basis of the model (Aziz and Settari, 1979). For a general phase k, we write

$$\frac{\partial}{\partial t}\left(\phi \rho_k S_k\right) + \nabla \cdot \left(\rho_k u_k\right) = Q_k \tag{1}$$

where the subscript k is interchanged by g or w to denote the gaseous or the aqueous phases, respectively, t is time, ϕ is the porosity of the porous medium, ρ_k is the mass density of the phase, S_k is the saturation of the phase, u_k is the superficial or Darcy velocity, and Q_k is the source/sink term that is used to apply boundary conditions.

In the case where the porous medium is not initially saturated with surfactant solution, an additional mass conservation equation on the surfactant is necessary. The surfactant transports as an adsorbing tracer with the water phase and, therefore, its conservation equation is written as

$$\frac{\partial}{\partial t}\left[\phi\left(C_s S_w + \Gamma\right)\right] + \nabla \cdot \left(u_w C_s\right) = Q_s \tag{2}$$

where C_s is the number or molar surfactant concentration in the aqueous phase, Γ is the amount of surfactant adsorption on the rock in units of moles per void volume, Q_s is the source/sink term for surfactant in units of moles/volume/time.

Almajid and Kovscek (2019) use a pore network model to show the importance of bubble texture to the foam displacement process. In their work, as the probability that a pore throat contains a lamella resulting from snap off, f_{so}, increases, so does the average bubble texture/density. Accordingly, the displacement becomes more uniform and travels like a shock through the network. Other foam models also emphasize the importance of texture to the accurate prediction of foam flow through the porous medium (Hirasaki and Lawson, 1985; Friedmann and Jensen, 1986; Falls et al., 1988; 1989; Ettinger and Radke, 1992; Ransohoff and Radke, 1988; Chambers and Radke, 1991; Kovscek et al., 1995; Chen et al., 2010). For these reasons and to model foam flow mechanistically, it is necessary to add one more conservation equation describing the
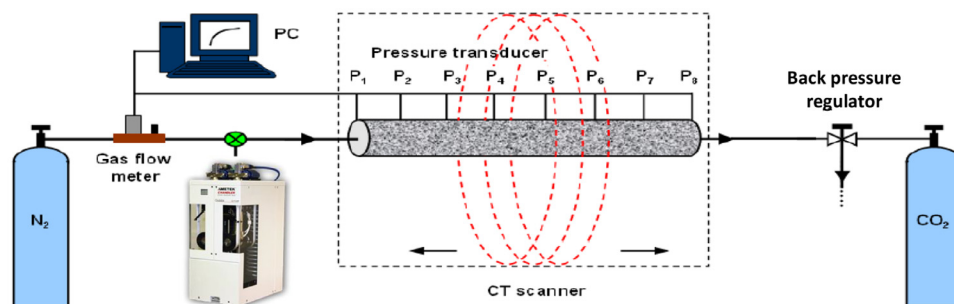

Fig. 2. Schematic of the experimental set up that is suitable for x-ray CT scanning.

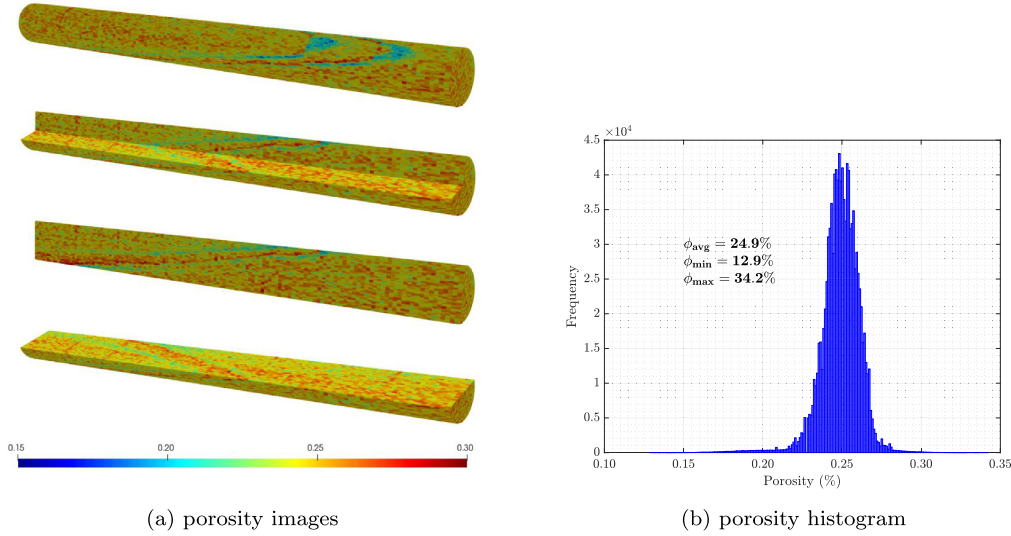(a) porosity images

(b) porosity histogram

Fig. 3. The porosity of the core as obtained from CT images using the fluid substitution method. (a) in situ porosity images along various axial sections where red is most porous and blue least, and (b) porosity histogram. Flow direction is from right to left. Note laminations (light blue shading) in the top left image.

flowing bubble density, n_f written as (Patzek, 1988)

$$\frac{\partial}{\partial t}\left[\phi\left(S_{gf}n_f + S_{gt}n_t\right)\right] + \nabla \cdot \left(u_g n_f\right) = \phi S_g \left(r_g - r_c\right) + Q_b \qquad (3)$$

where subscripts f and t denote the flowing and trapped gas, respectively. n_f is the flowing bubble density per unit volume of flowing gas and n_t is the trapped bubble density per unit volume of the trapped gas.

The first term on the left hand side of Eq. (3) is the accumulation of the bubbles. The second term represents the convection of foam bubbles that travel with the gas phase. On the right hand side of Eq. (3), the first term represents the net generation of foam. The rate of generation, r_g, and the rate of coalescence, r_c, are represented on a per volume of gas basis. Lastly, Q_b is a source/sink term of bubbles.

In the case where no pregenerated bubbles are injected into the porous medium, this source term is set to zero. In its presence or absence, the kinetic expressions of r_g and r_c determine the evolved bubble texture in the porous medium. The importance of these kinetic expressions is appreciated by recognizing that at steady-state away from any sources or sinks, the evolved bubble texture is determined by equating the rate of generation to the rate of coalescence ($r_g = r_c$) (Ettinger and Radke, 1992). Furthermore, the assumption of bubble texture being set entirely by the instantaneous balance between generation and coalescence was used to model transient foam flow successfully (Chen et al., 2010). In this paper, we use the full-physics model without any relaxation of the problem. We present a relaxed form of the full-physics model elsewhere and show that it is possible to obtain meaningful results with less computational cost (Almajid, 2019). The final residual form of the conservation equations described in this section that were incorporated into AD-GPRS are shown in the Supporting Information.

4.2. Rates of generation and coalescence

There are several mechanisms by which foam is generated in a porous medium. Ransohoff and Radke (1988) observed: snap-off, lamella division, and leave-behind. Liontas et al. (2013) add two more neighbor-induced pinch-off mechanisms. All of these mechanisms lead to stronger foam generation with some dominating over others. Almajid and Kovscek (2019) compute the likelihood of snap-off in a cubic pore network to be larger than the likelihood of lamella division. For this particular reason, we chose snap-off to be the mechanism responsible for foam generation in our model. Consonant with the above arguments, the rate of generation formulation we chose is similar to that

used by Chen et al. (2010) and is applicable for the low- and high-quality regimes

$$r_g = k_1^0 \left(1 - \left(\frac{n_f}{n^*}\right)^\omega\right) \bar{v}_w \bar{v}_g^{1/3} \qquad (4)$$

where k_1^0 is taken to be a constant, ω is a constant determining the shape of inverse proportionality of foam germination sites to preexisting gas bubbles. Throughout this paper, we use a value of 3 for ω based on the sensitivity study of Chen (2009).

As opposed to germination sites where lamellae are created, termination sites are where lamellae break and thus bubbles coalesce. The stability of a lamella depends on the surfactant properties, surfactant concentration, liquid saturation, rock type, and how fast the lamella traverses the pore (Khatib et al., 1988; Jimenez and Radke, 1989; Kahrobaei and Farajzadeh, 2019). Surfactant/rock interactions dictate how much surfactant is lost from the lamella to the rock surface. Additionally, the balance between the lamella's disjoining pressure and the capillary pressure of the surrounding region determines the rate by which coalescence happens. Rapidly-moving lamellae do not have enough time to heal as they stretch and rupture is inevitable (Jimenez and Radke, 1989). Based on these arguments, we choose the rate of coalescence to be

$$r_c = k_{-1}^0 \left(\frac{P_c}{P_c^*(C_s) - P_c}\right)^2 \bar{v}_g n_f \qquad (5)$$

where k_{-1}^0 is taken to be a constant. Moreover, the work of Aronson et al. (1994) on various aqueous surfactants suggests the following functional form for P_c^* as a function of C_s

$$P_c^*(C_s) = P_{c,max}^* \tanh\left(\frac{C_s}{C_s^*}\right) \qquad (6)$$

where $P_{c,max}^*$ is a maximum value for P_c^*, and C_s^* is a reference surfactant concentration for strong net foam generation. The capillary pressure of the porous medium is approximated using the Leverett J-function (Kovscek et al., 1995). The exact formula is defined in the Supporting Information.

4.3. Phase mobilities

In addition to the governing equations and the foam kinetic expressions for generation and coalescence, additional flow rate relationships for the wetting and the gas phases are necessary to complete the model.

We use the multiphase extension of Darcy's law

$$u_k = -\frac{Kk_{rk}}{\mu_k}\nabla\left(p_k + \rho_k gz\right) \tag{7}$$

where K is the absolute permeability, k_{rk} is the relative permeability of phase k, μ_k is its viscosity, p_k is its pressure, ρ_k is its density, g the gravitational constant, and z is the depth.

Accordingly with the pore-scale depiction of foam shown in Fig. 1, the wetting liquid mobility is unaffected by the presence of the bubbles as the wetting phase maintains continuity in the pore space. Thus, the viscosity of the wetting liquid is set to be a constant and a modified Corey-type is used to describe its relative permeability as described by Kovscek et al. (1995).

The discontinuity of the gas phase suggests that its mobility is affected by the presence of foam. Thus, the gas mobility is adjusted accordingly. The gas viscosity is, hence, replaced with an apparent gas viscosity in the presence of foam. Flowing bubbles do not exhibit a Newtonian viscosity because they lay down thin lubracting films on the pore walls as they move in the pore space (Hirasaki and Lawson, 1985). Therefore, the apparent viscosity of gas in the presence of foam, μ_f, is written as

$$\mu_f = \mu_g + \frac{\alpha n_f}{\bar{v}_g^{1/3}} \tag{8}$$

where μ_g is the gas viscosity in the absence of foam, α is a constant of proportionality that is dependent on the surfactant system, n_f is the bubble density, and v_g is the local interstitial gas velocity. The apparent viscosity increases with bubble density, but it is shear thinning at constant bubble densities.

Because not all of the gas phase is mobile during foam flow (Gillis and Radke, 1990; Cohen et al., 1997; Kharabaf and Yortsos, 1998; Tang and Kovscek, 2006; Almajid and Kovscek, 2019), the gas-phase relative permeability in the presence of foam must be adjusted. Similar to the wetting liquid phase, we adopt a modified Corey-type relative permeability description but adjust the gas-phase relative permeability to account for the fraction of the gas phase actually flowing. The flowing foam fraction, X_f ($= S_{gf}/S_g$), is introduced as done by previous studies (Kovscek et al., 1995). The expression of X_f used is that proposed by Tang and Kovscek (2006), that is written as

$$X_f = \psi\left[\frac{\nabla p_g}{n_f K^{1/2}}\right]^g \tag{9}$$

where ψ is a constant of proportionality, and g is a percolation exponent that is taken to be equal to 0.4 because our core represents a large 3D pore network. The expression captures the fact that the flowing foam fraction increases when the applied pressure gradient increases, the bubble density decreases, or the permeability decreases (Kharabaf and Yortsos, 1997; Chen et al., 2006; Almajid and Kovscek, 2019). For a more detailed descriptions about the specific forms used for the relative permeability of the gaseous and aqueous phase as well as the origin of the form that the flowing foam fraction takes, please refer to the Supporting Information.

5. Numerical implementation

5.1. AD-GPRS

The mechanistic foam model developed above was implemented in the Automatic Differentiation General Purpose Research Simulator (AD-GPRS) framework (Voskov and Tchelepi, 2012; Zhou et al., 2011; Zhou, 2012). The governing equations in residual form that were included in AD-GPRS are included in the Supporting Information. AD-GPRS provides flexibility to solve multiphysics problems as it has a general implicit coupling framework (Rin et al., 2017). The framework is modular where a multiphysics problem can be split into subproblems. Each subproblem represents particular physics. For this paper, we add a foam subproblem and use the already implemented flow problem. Adding a

foam subproblem to such a modular and flexible framework is a first step to modeling more complex physical processes that include foam physics such as steam foams that might employ the flow, foam, and thermal subproblems.

We use the fully implicit method (FIM) for time approximation. Because we found the foam problem to be very stiff, we use a sequential structure as a type of nonlinear preconditioner to compute a good initial guess for the fully coupled, fully implicit multiphysics problem. This approach is similar to the work done by Wong et al. (2018, 2019) for a geothermal energy problem. Our general scheme is to first solve for flow alone while holding the bubble density constant, then use that solution as a constant and solve for bubble density alone, and finally combine the two problems to find the final solution. In other words, we solved for each individual physics subproblem separately first to provide a good initial guess to the fully coupled problem.

A key challenge to the implementation of the mechanistic foam model is the computation of the apparent gas-phase viscosity when foam is present (Hirasaki and Lawson, 1985). The apparent gas viscosity when foam is present depends on the flowing bubble density as well as the interstitial velocity of the gas. Both of these variables change with space and time as the pressure as well as the saturation of each block evolves. The following section describes in detail our implementation of this important variable in our model.

5.2. Computing apparent gas viscosity

We use the bisection method to compute the effective viscosity as a function of the primary variables (pressure, water saturation, and bubble density). So a bisection method is applied to solve $F(p, S_w, n_f, \mu_f) = 0$ for a given p, S_w, n_f

$$F(p, S_w, n_f, \mu_f) = M_f(p, n_f, S_w, \mu_f) - \mu_f = 0 \tag{10}$$

where $M_f(p, n_f, S_w, \mu_f)$ is the procedure to compute the effective gas-phase viscosity as a function of primary variables and can be obtained by rearranging Eq. (8) to get

$$M_f(p, n_f, S_w, \mu_f) = \mu_g + \frac{\alpha n_f}{\mu_g^{1/3} v_g^{1/3}}\mu_f^{1/3} \tag{11}$$

where μ_g is the unfoamed gas viscosity, and v_g is the gas velocity that is still not yet affected by the bubbles at the current timestep. Thus, the function to compute the gas-phase effective viscosity as a function of our primary variables is written as

$$\mu_f^{\text{value}}(p, S_w, n_f) = \text{BISECTION}(F(p, S_w, n_f, \mu_f)). \tag{12}$$

M_f the procedure to compute the effective gas viscosity as a function of primary variables

Once we have the viscosity, the next step is to ensure that the derivatives are properly computed. This ensures that the derivatives of all the other properties dependent on the foam viscosity are correctly computed.

The derivative computation is based on the Inverse Function Theorem, which states that

$$\frac{dY}{dX} = -\left(\frac{dF}{dY}\right)^{-1}\frac{dF}{dX} \tag{13}$$

where

$$F(X, Y) = 0 \tag{14}$$

Because we are interested in computing the effective gas viscosity derivative with respect to the primary variables, we apply the Inverse Function Theorem for $Y := \mu_f$, $X := (p, S_w, n_f)$, and

$$F(X, Y) = F(p, S_w, n_f) = M(p, S_w, n_f) - \mu_f = 0 \tag{15}$$

Once the ADscalar effective gas viscosity value and derivatives are computed for each cell, all other properties are evaluated. The derivatives all have the correct derivatives because they are all a function of our primary variables (p, n_f, S_w).

5.3. Numerical issues with rate of coalescence

One issue that could hinder the efficiency of the numerical implementation is the quadratic form of the rate of coalescence especially during high gas fractional flow runs. As the gas saturation of a grid block increases, so does its P_c. If P_c is the same as or greater than P_c^*, we run into numerical problems. In the case that they are equal, there exists a discontinuity. We resolve this by adding a small value ($\epsilon = 1 \times 10^{-8}$) to ensure that the difference is always positive. On the other hand, when P_c is greater than P_c^*, then the rate of coalescence decreases because of the quadratic form used, which is incorrect. This same numerical issue makes optimizing foam simulators to deduce parameters difficult (Ma et al., 2019). To resolve this issue, one could multiply the constant of rate of coalescence by a very large number to indicate chaotic coalescence that is typically reported in this regime. Another method to overcome this issue is to linearly extrapolate the value that one would get if the difference between P_c^* and P_c was ϵ based on their actual difference. We opted to use the first method because it simplifies the implementation. More work needs to be done to study as well as to resolve this issue in the future.

6. Model predictions of foam flow

Foam flow in porous media is extremely nonlinear and has many interesting behaviors. In this section, we test the validity of the full-physics, mechanistic model developed here to predict both the steady-state and transient behaviors. We qualitatively show that the model is able to predict the two flow regimes that are usually observed in steady-state foam flow experiments (Osterloh and Jante, 1992). Then, we use several transient experimental data to compare and validate our model results. For transient foam flow, we compare our quantitative predictions to four experimental datasets. Two of the data sets are homogeneous cases from the literature and are included in the Supporting Information. The experimental data in the Supporting Information validate the model results against cases when the initial saturation condition is altered. On the other hand, the experimental data in the main paper compares the model's predictions versus results from the heterogeneous sandstone core sample, Fig. 3.

6.1. Steady-state foam flow

Steady-state pressure gradient measurements during foam flow yield interesting behavior. Osterloh and Jante (1992) measure the steady-state pressure gradient along a sandpack and report that foam exhibits two regimes depending on the injection conditions. They report the steady-state pressure gradient to be independent of gas velocities and dependent on liquid velocities when the gas fractional flow is large. They coin this regime as the high-quality regime. On the other hand, their data show that the steady-state pressure gradient is independent of the imposed liquid velocity but dependent on the gas velocity when the gas fractional flow is low. They coin this regime as the low-quality regime. The transition between the two regimes occurs in their experiments at a foam quality (gas fractional flow) of 94%. Alvarez et al. (2001) further confirm these results by measuring steady-state pressure gradient along cores and sandpacks with various surfactant formulations and gases. They conclude that the transition foam quality depends on the permeability of the porous medium. Cores exhibit smaller transition foam qualities than sandpacks. This is attributed to differences in the details of capillary pressure between consolidated and unconsolidated rocks.

Fig. 4 presents our model predictions of the steady-state pressure gradients as a function of the gas and the liquid Darcy velocities using the parameters in Table S1 in the Supporting Information. When the liquid Darcy velocity is small (less than 1.0 m/day), the pressure gradient is insensitive to the gas velocity but sensitive to the liquid velocity.
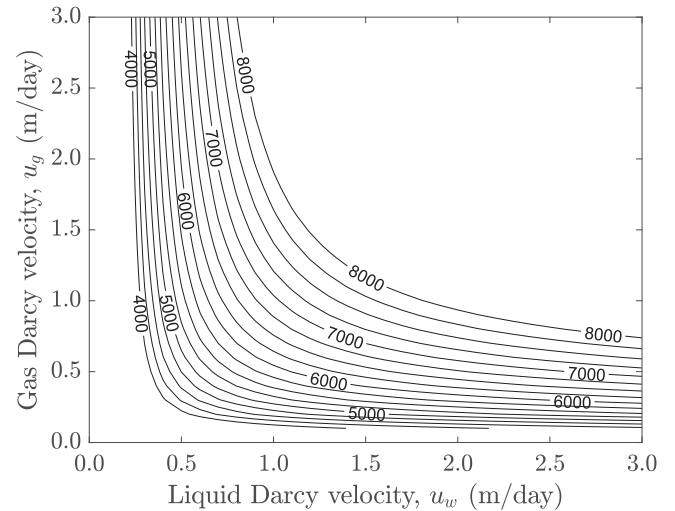

Fig. 4. Model predictions of steady-state pressure gradient, ∇p, contours in (kPa/m) as a function of gas Darcy velocity, u_g, and water Darcy velocity, u_w.
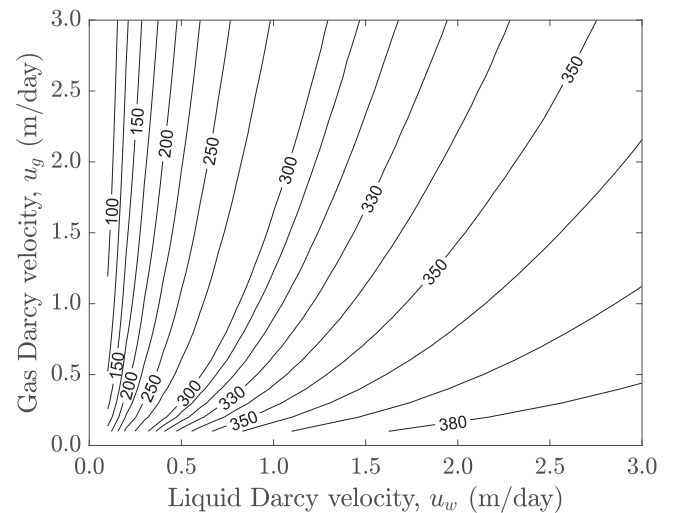

Fig. 5. Model predictions of steady-state bubble density, n_f, contours in (mm^{-3}) as a function of gas Darcy velocity, u_g, and water Darcy velocity, u_w.

Conversely, when the liquid velocity is large, the pressure gradient increases with the gas velocity but remains constant with respect to the liquid velocity. This seems to be in accordance with the experimental observations in the literature (Osterloh and Jante, 1992; Alvarez et al., 2001).

The steady-state average bubble density predictions are plotted as a function of the gas and liquid Darcy velocities in Fig. 5. The average bubble density depends on the liquid velocity. When the liquid velocity is small, the average bubble density appears insensitive to the gas velocity. As the liquid velocity increases, the average bubble density is a function of both gas and liquid velocities. Larger liquid velocities make the foam bubbles finer but larger gas velocities coarsen the foam bubbles. This seems to be in agreement with theory as the generation rate varies linearly with the liquid velocity (Persoff et al., 1989; Kovscek and Radke, 1996; Almajid, 2019) while the coalescence rate increases as the gas velocity increases (Jimenez and Radke, 1989).

6.2. Transient foam flow heterogeneous, $f_g = 50\%$

In this example, we model a low-quality regime experiment in the slightly heterogeneous core sample. Gas and foamer solution are

Table 1
Model parameters used for transient foam flow calculations.

Two-phase flow parameters		Population balance parameters	
Parameter	Value	Parameter	Value
K	0.55 μm^2	k_1^0	2.24×10^{14} m$^{-13/3}$ s$^{1/3}$
ϕ	0.25	k_{-1}^0	1.5 m^{-1}
k_{rw}^0	1.0	$P_{c,max}^*$	3.0×10^4 Pa
k_{rg}^0	0.70	α	3.35×10^{-17} Pa-s$^{2/3}$-m$^{10/3}$
S_{wc}	0.25	ψ	varying
μ_w	1.0×10^{-3} Pa-s	C_s^*	0.083 wt%
μ_g	1.8×10^{-5} Pa-s	n^*	4×10^{11} m^{-3}
a	0.022		
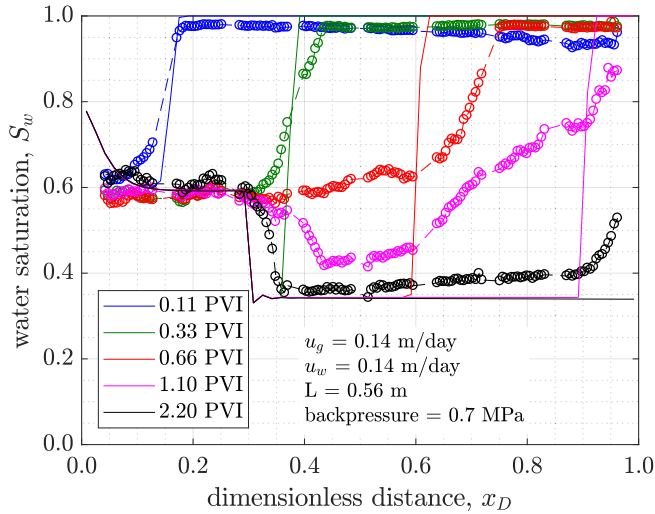
Fig. 6. Experimental (symbols) and model (lines) transient water saturation profiles. The heterogeneous porous medium is presaturated with foamer solution. Gas fractional flow is 50%.

Fig. 7. Experimental (symbols) and model (solid lines) transient pressure-drop profiles. Dashed lines connect pressure-drop measurements. The heterogeneous porous medium is presaturated with foamer solution. Gas fractional flow is 50%.

injected into a core that is completely saturated with foamer solution. Gas is injected at a Darcy velocity of 0.14 m/day relative to the applied backpressure of 0.7 MPa, while the foamer solution is injected at a Darcy velocity of 0.14 m/day. The resultant foam quality is 50% at the core exit. Because CT images of the core show two lower-permeability layers sandwiching a higher-permeability layer, we expect the behavior of the pressure, saturation, and bubble density to be different than the validation cases in the Supplementary Information. Table 1 lists the model parameters for the heterogeneous cases.

Measured aqueous-phase saturation profiles as well as measured pressure profiles indicate that the foam generated in the experiment was relatively weak until a dimensionless distance of 0.3. Having observed this, we alter the flowing foam fraction in our model and make it discontinuous along the core. More precisely, we assign each grid a value of the constant of proportionality, ψ, in Eq. (9). In this example, the assigned ψ value is larger in the first 0.3 dimensionless distance of the core. Having a larger constant of proportionality indicates that foam flows more easily and, hence weak foam is formed even after foam generation.

Fig. 6 plots the aqueous-phase saturation profiles at varying dimensionless times. At the first three dimensionless times (i.e. 0.11 PVI, 0.33 PVI, and 0.66 PVI), the gas moves into the core quickly draining a considerable amount of liquid (0.4 units of saturation). Measured data show that strong foam starts to generate somewhere around dimensionless distance of 0.3. Predicted aqueous-phase saturation tracks the advancement of the two dimensionless times well. The model predicts slower front advancement at 0.66 PVI and 1.10 PVI. This is attributed to the higher-perm layer that the free-gas preferentially flows through if it is not foamed. Even considering this heterogeneity in the core, the model
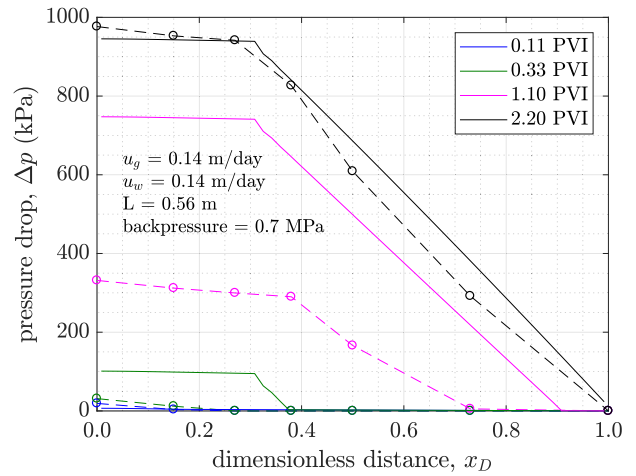
tracks roughly the position of the measured front. Additionally, steady-state is reached after 2.20 PVI that is matched to a good agreement by the numerical model.

A foam's strength is not only gauged by the resultant aqueous-phase saturation but also by the resultant pressure gradient it builds. Fig. 7 shows the predicted and measured pressure profiles at four dimensionless times. Consonant with the saturation measurement, the model predicts early times and steady-state well and mismatches the times in between. Again, the mismatch between the model and experiments at intermediate times is attributed to the heterogeneity of the core that affects the amount of gas in the core and the manner by which it resides inside the core. From a closer examination of Figs. 6 and 7 at a time of 1.10 PVI, we observe that the amount of gas estimated by the model is larger than the actual experiment. The discontinuous drop in S_w occurs at a greater distance from the inlet experimentally than numerically. Second, after the discontinuous drop in S_w, the gas travels in a piston-like fashion meaning that it develops a strong foam but that is not necessarily the case experimentally. The experiment shows a smeared front rather than a piston-like displacement consistent with the subcore scale heterogeneity in Fig. 3(a). A more piston-like displacement translates into a larger pressure drop developed. Hence, there is difference in intermediate pressure drop estimations by the model.

The larger aqueous-phase saturation and the shallow pressure gradient in the weak foam region (i.e. dimensionless distance less than 0.3) are achieved by using a discontinuous value of the constant of proportionality in the expression for flowing foam fraction, as discussed above. The flowing foam fraction that results from the model is shown in Fig. 8. Larger values of X_f lead to larger gas relative permeability values and, hence, larger aqueous-phase saturation. For instance, Fig. 6 shows a larger aqueous-phase saturation near the inlet of 0.8 that corresponds to a flowing foam fraction of 1.0. When the foam is weak, we expect easier mobilization and vice versa. The local minima in the X_f profile at the displacement front coincide with the regions of large net foam where the bubble density is large, Fig. 9.

One interesting feature about Fig. 9 is the average bubble density upstream and downstream of the X_f discontinuity. Almajid (2019) uses the pore network of Almajid and Kovscek (2019) to capture qualitatively the aqueous-phase saturation behavior observed in these experiments using two snap-off probabilities, f_{so}, upstream and downstream of the discontinuity. A larger f_{so} downstream of the discontinuity represented stronger foam and finer texture. The reported mean bubble densities in Fig. 9 upstream and downstream of the discontinuity (n_f^- and n_f^+) seem to be in agreement with our qualitative results. The average bubble density is larger where foam is stronger.
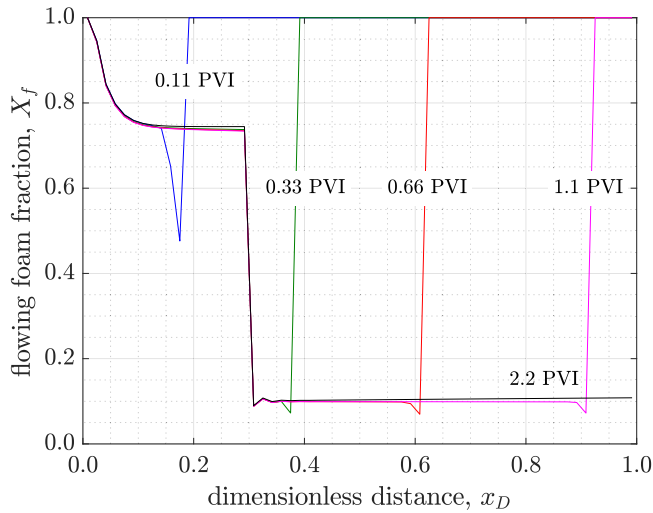
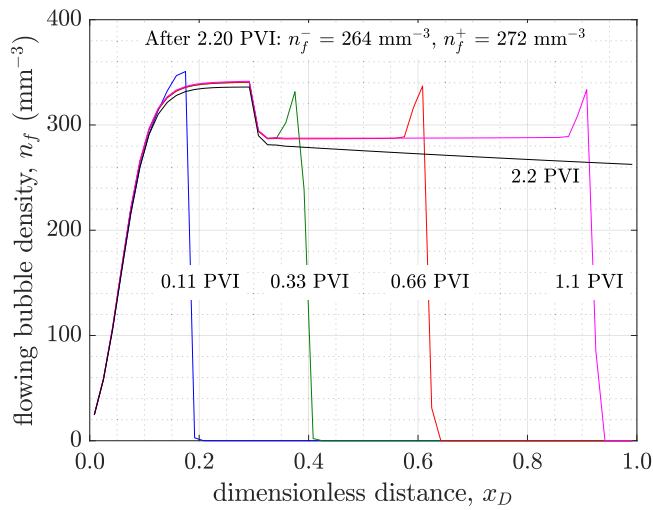**Fig. 8.** Model transient flowing foam fraction profiles. Gas fractional flow is 50%.

Fig. 9. Model transient bubble density profiles. Gas fractional flow is 50%.

Fig. 10. Experimental (symbols) and model (solid lines) transient water saturation profiles. The heterogeneous porous medium is presaturated with foamer solution. Gas fractional flow is 90%.

Fig. 11. Experimental (symbols) and model (solid lines) transient pressure-drop profiles. Dashed lines connect pressure-drop measurements. The porous medium is presaturated with foamer solution. Gas fractional flow is 90%.

6.3. Transient foam flow, heterogeneous, $f_g = 90\%$

In this example, we model a high-quality regime experiment in the same slightly heterogeneous core sample. Gas and foamer solution are injected into a core that is completely saturated with foamer solution. Gas is injected at a Darcy velocity of 1.90 m/day relative to the applied backpressure of 0.7 MPa, while the foamer solution is injected at a Darcy velocity of 0.21 m/day. The resultant foam quality is 90% at the core exit. The main difference between this experiment and the previous one is only the gas fractional flow applied.

Fig. 10 plots the aqueous-phase saturation against dimensionless distance for four dimensionless times. The model tracks the front well in the early times (i.e. less than 1.28 PVI). The wetting liquid saturation is underestimated by the model in the weak foam region (i.e. below dimensionless distance of 0.5). Interestingly, the front is less smeared after passing the discontinuity at dimensionless distance of 0.5.

The pressure profiles of three dimensionless times are shown in Fig. 11. Similar to the 50%-quality foam, the model approximates the pressure profile well in the very early times and at steady state but mismatches the experimental results in intermediate times after the foam front passes the discontinuity in the core. The mismatch in this case is less severe because the drier foam presents less smearing in the foam front in intermediate times.
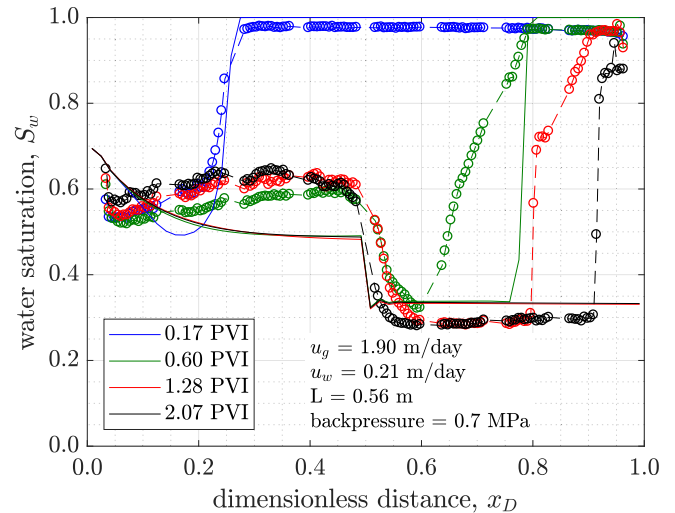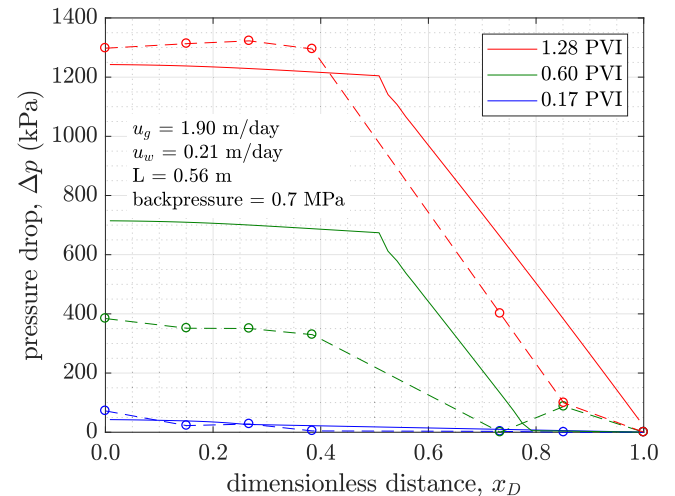
Again, we use a discontinuous flowing foam fraction to capture the large aqueous-phase saturation and shallow pressure gradients upstream of the discontinuity in dimensionless distance 0.5. The resulting flowing foam fraction is shown in Fig. 12. The local minima in X_f at the displacement front are due to the region of large net foam generation near the foam front, as explained in the previous case.

We also report the average bubble density in this case before and after the discontinuity in Fig. 13. The general magnitude of predicted foam texture, 200 to 300 mm^{-3}, agrees with the measurements of Chen et al. (2010) under similar surfactant and flow-rate conditions in a permeable sandstone. Observations made with respect to Fig. 9 also generally apply here. The more interesting observation is that mean values of texture are smaller than the low-quality foam case. For example the texture at a position of $x_D = 0.8$ is roughly 260 mm^{-3} at a time of 2.2 PVI in Fig. 8 whereas the texture is 180 mm^{-3} at the same position at 2.1 PVI in Fig. 12. This makes sense because wetter foams have larger relative liquid velocities as compared to the gas liquid velocities and, hence, snap-off could occur more frequently there.
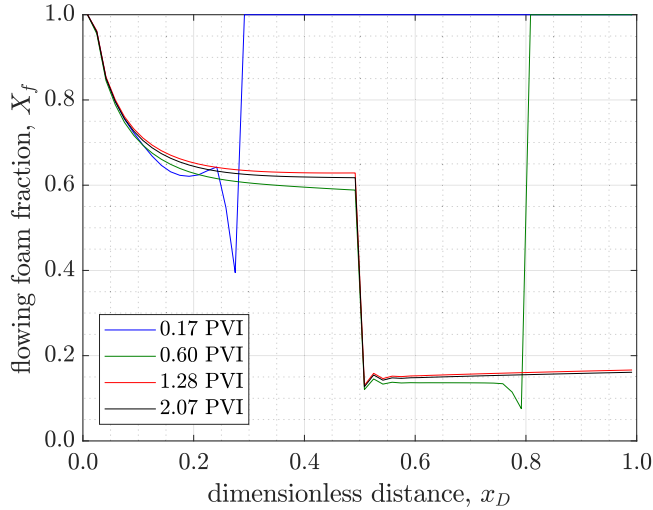
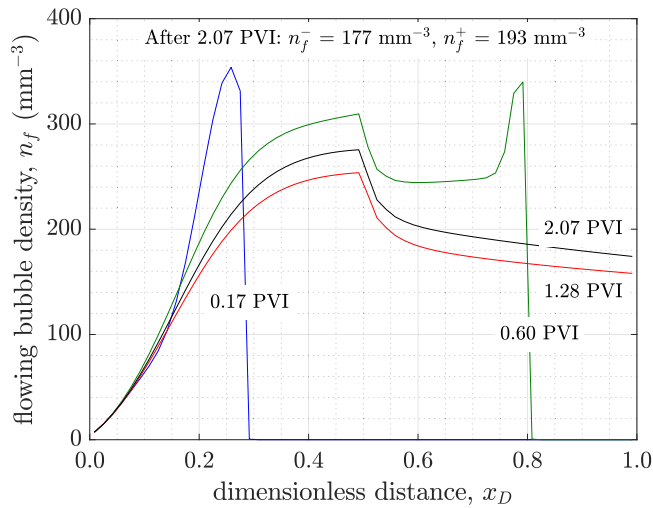**Fig. 12.** Model transient flowing foam fraction profiles. Gas fractional flow is 90%.

Fig. 13. Model transient bubble density profiles. Gas fractional flow is 90%.

7. Discussion

The gas flux is not necessarily a monotone function during these simulations. This discussion explores monotonicity, the prospects for scale up of the simulation approach to larger domains, and the extension of the model to include NAPL destablizating effects. For a discussion of 2D simulations and the role of heterogeneity, the reader is encouraged to check the S4 in the Supporting Information that justifies the use of 1D simulations as an approximation of the 2D results.

7.1. Monotonicity in the gas flux function

To examine the presence of or the absence of monotonicity in the gas flux function during foam flow, we plot the gas flux function given different mobility ratios. The gas fractional flow is defined as:

$$f_g = \frac{1}{1 + \lambda_w/\lambda_g} \tag{16}$$

where f_g is the gas fractional flow, $\lambda_w = (k_{rw}/\mu_w)$ is the aqueous-phase mobility in units of cp^{-1}, and $\lambda_g = (k_{rg}/\mu_g)$ is the gaseous-phase mobility in units of cp^{-1}. We alter the gaseous-phase mobility by increasing the gas effective viscosity, μ_g^f, in the presence of foam. For example, a strong foam exhibits an effective viscosity that is 100 times larger than the gas
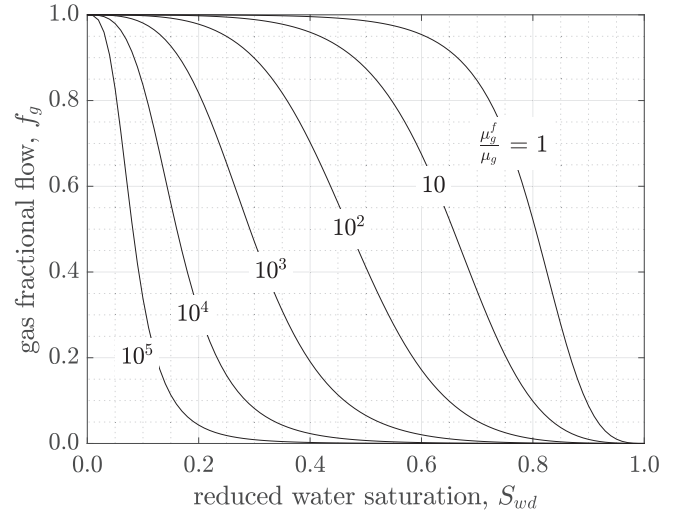

Fig. 14. Theoretical gas flux functions with increasing foam strength. Each curve represents the gas fractional flow given a certain mobility modification through changing the gas viscosity. Strong foam increases the gas apparent viscosity significantly.
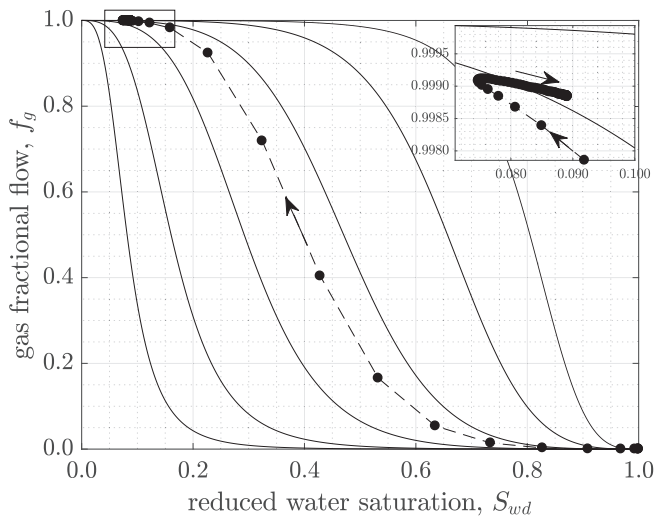
viscosity and follows the gas fractional flow curve indicated by $\mu_g^f/\mu_g = 10^2$ in Fig. 14. Thus, foam strength increases going from the right-most curve to the left-most curve in that figure.

We first use the parameters and the simulation results of the transient foam flow experiment in heterogeneous media presaturated with surfactant solution in the Supporting Information to examine the monotonicity of the gas flux function in a porous medium that is initially fully-saturated with foamer solution. We use a 1D model that has 240 grid blocks and refine timesteps to be able to see the saturation changes with time. Fig. 15 shows the gas fractional flow that is exhibited by two grid blocks. Grid block #5 is close to the injection point while grid block # 20 is away from the injection point and represents how gas fractional flow behaves in the rest of the grid blocks away from the injection point.
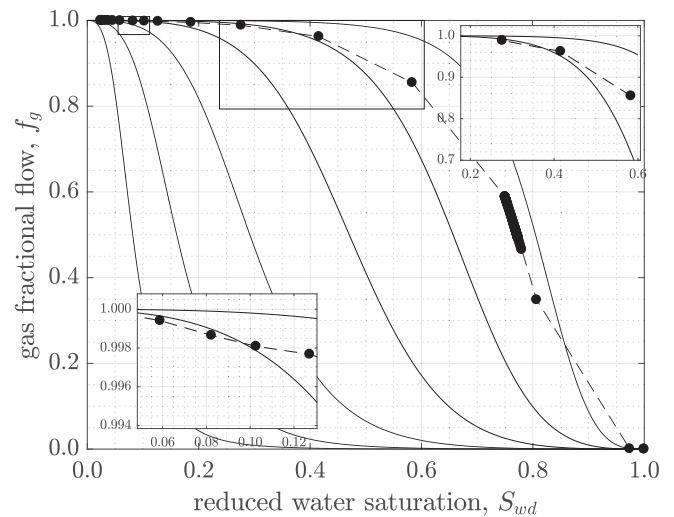
Fig. 15 a and b show that the gas flux function is nonmonotonic when the porous medium is initially fully-saturated with foamer solution. Initially, the gas flux function increases monotonically as the bubble density increases and as the water saturation decreases. Because of the relative increase in the bubble density caused by net foam generation at the foam front, the gas flux function is nonmonotonic as evidenced by the zoomed-in figures. The water saturation as well as the gas fractional flow decrease as the bubble density profiles equilibrate.

The next case we examine is transient foam flow where the homogeneous porous medium is initially fully-saturated with brine. Similarly, we show two grid blocks, one close to the injection side, Fig. 16a, and another one that is farther from the injection point and represents how the rest of the grid blocks behave, Fig. 16b. The model in this case is much finer than the previous case and has 1920 grid blocks. The gas flux function in this case increases monotonically. Examining the flowing bubble density profiles of this case shows no region of net foam generation and a relative increase of foam texture similar to the previous case. This observations seems to explain why the gas flux function is monotonic in this case. As a point of clarification, there is no region of net foam generation because surfactant concentration is also transient in this case. Hence, the surfactant concentration is relatively small at the foam front and conditions are not favorable for net foam generation.
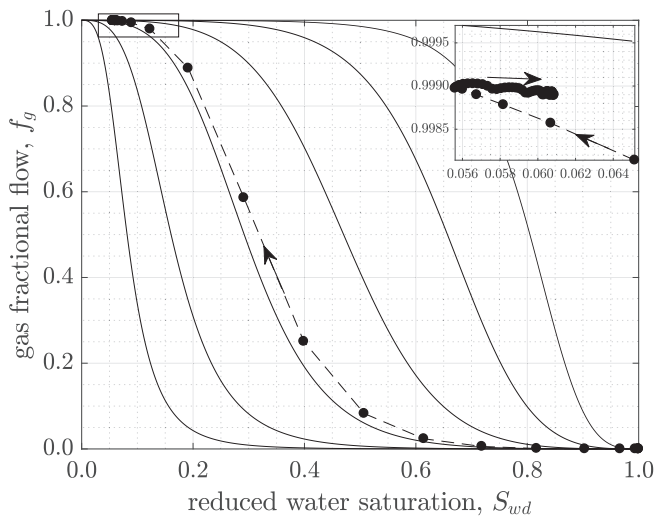
When comparing the previous two cases, we observe another interesting behavior. When the porous medium is initially fully-saturated with foamer solution, the gas mobility is modified such that the gas flux function follows only one curve out of all possible curves except at late times where nonmonotonic behavior is witnessed. The situation is distinctly different and more interesting in the case where the porous medium is initially fully-saturated with brine (i.e., contains no surfac-
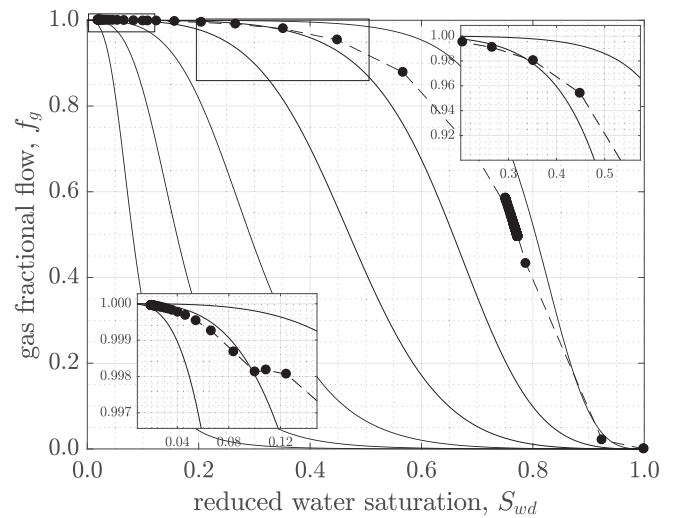
(a) grid block #: 5

(b) grid block #: 20

Fig. 15. Nonmonotonic gas flux functions when the porous medium is initially saturated with foamer solution. Arrows indicate the saturation path during the simulation run in two different grid blocks during a simulation. Circles represent simulation results while solid lines are theoretical.

(a) grid block #: 98

(b) grid block #: 240

Fig. 16. Monotonic gas flux functions when the porous medium is initially saturated with brine in two different grid blocks during a simulation. Circles represent simulation results while solid lines are theoretical.

tant). In that case, the initial free gas ineffectively drains the medium to a large water saturation while the gas mobility follows that of an unfoamed-gas. However, as soon as the gas is foamed, the gas flux function jumps from one gas fractional flow curve to the other as the gas mobility is further modified. The zoomed-in figures of both Fig. 16a and b show the intersection points between the respective grid block gas fractional flow curve and the theoretical curves.

7.2. Scale up to larger domains

The mechanistic model developed and tested above performs well against experimental data especially in homogeneous rock samples at the meter scale. There are, however, some challenges that need to be circumvented before we take this further to 10's of meter scale. We believe that heterogeneity plays a vital and pivotal role in any foam flow process and is inevitable to be encountered in nature. Therefore, a key step that needs further investigation is the integration of the heterogeneity found in rock samples. This may be accomplished by introducing rock classes, in which each class has differing multiphase properties (i.e. relative permeability curves, capillary pressure curves, apparent viscosity

behavior). A version of this idea for fractured media was implemented by Pancharoen et al. (2012). Their work needs to be extended to include capillary pressure and relative permeability differences in each rock type and then be implemented within our model to move to larger length scales.

The other issue is the implementation of wells in larger-scale domains. This is due to the fact that foam viscosity exhibits a shear-thinning behavior. A 10's of meter scale simulation could have grid blocks that are much larger than the wellbore, hence a large difference between the bottom hole flowing pressure and a grid block's pressure is expected. A significant difference in pressure would lead to shear-thinning behavior between the wellbore and the grid block. Li et al. (2006) circumvent this issue through adding a negative, viscosity dependent apparent viscosity skin factor in the well model to accommodate the non-Newtonian effects between the wellbore and the grid block.

7.3. Extension to include NAPL destabilizing effects

The model in this paper captures foam generation and coalescence mechanisms in the absence of mobile NAPLs. Hence, the model is

suitable for applications in the absence of NAPLs or in the presence of residual NAPLs. It is, however, well documented that NAPLs have a destabilizing effect on foam (Farajzadeh et al., 2012; Almajid and Kovscek, 2016; Schramm and Novosad, 1990; Manlowe and Radke, 1990; Myers, 1999; Myers and Radke, 2000; Bergeron et al., 1993). Because the population balance model is implemented in the AD-GPRS framework, it allows a straightforward extension to include such effects. For instance, following the work of Myers and Radke (2000), a third reaction term that accounts for coalescence of foam due to the presence of NAPLs, r_{co}, needs to be included. The term that Myers and Radke (2000) included in their work was a function of the bubble flux, $\bar{v}_g n_f$, the NAPL saturation, S_o, the imposed capillary pressure on a pseudoemulsion film, $P_{c_{pf}}$, and the rupture capillary pressure of a pseudoemulsion film, $P_{c_{pf}}^*$. Additionally, $P_{c_{pf}}$ depended on the NAPL/water and gas/water capillary pressures, and the surface tensions of the system. All of these parameters, once defined, can be implemented to compute a third reaction term that adds the destabilizing effect of NAPLs on foam.

8. Concluding remarks

This paper illustrates the development and implementation of a mechanistic, full-physics population balance transient foam flow model into the multiphysics, modular AD-GPRS simulator. The automatic differentiation capabilities significantly aid efforts to prototype expressions of physical phenomena. We propose a new flowing foam fraction function and extend an existing population balance model to predict experimental data in homogeneous and slightly-heterogeneous porous media. In the homogeneous cases, we find that the model predicts well the measured data. The model predictions were compared to constant surfactant concentration as well as transient surfactant flow cases. Qualitatively, our model predicts the two foam flow regimes usually reported in steady-state foam flow literature: low-quality foam and high-quality foam.

In the slightly-heterogeneous cases, our model tracks well the location of the saturation front and the steady-state and the early-time pressure and aqueous-phase saturation profiles. The intermediate-time pressure profiles are overestimated due to the difference of the amount of gas in the system between the model and experiments. The heterogeneous cases were predicted with a discontinuous flowing foam fraction function that is consonant with the steady-state results of Almajid et al. (2019). The model also predicts larger averaged bubble density when the gas has passed the high-low permeability barrier confirming results of previous pore network studies (Kharabaf and Yortsos, 1998; Almajid and Kovscek, 2019). Furthermore, we have shown that foam flow in porous media is nonmonotonic when the porous medium is presaturated with surfactant solution and that the nonmonotonicity disappears when it is initially brine-saturated.

Implementation of the foam population balance model in the modular, multiphysics AD-GPRS simulator provides a first step into modeling more complex and larger-scale processes in the future. For instance, mechanistic foam flow simulation at aquifer scale may be conducted. Additionally, steamfoam physics could be captured theoretically if the flow, foam, and thermal subproblems are coupled in AD-GPRS.

Declaration of Competing Interest

The authors declare that they have no known competing financial interests or personal relationships that could have appeared to influence the work reported in this paper.

CRediT authorship contribution statement

Muhammad M. Almajid: Methodology, Investigation, Software, Writing - original draft. **Zhi Yang Wong:** Methodology, Investigation,

Software. **Anthony R. Kovscek:** Conceptualization, Methodology, Supervision, Funding acquisition, Writing - review & editing.

Supplementary material

Supplementary material associated with this article can be found, in the online version, at doi:10.1016/j.advwatres.2021.103877.

References

Almajid, M.M., 2019. Experimental and numerical evaluation of foam physics in porous media across multiple scales. Ph.D. thesis.
Almajid, M.M., Kovscek, A.R., 2016. Pore-level mechanics of foam generation and coalescence in the presence of oil. Adv. Colloid Interface Sci. 233, 65–82.
Almajid, M.M., Kovscek, A.R., 2019. Pore network investigation of trapped gas and foam generation mechanisms. Transp. Porous Media 1–25.
Almajid, M.M., Nazari, N., Kovscek, A.R., 2019. Modeling steady-state foam flow: Hysteresis and backward front movement. Energy Fuels 33 (11), 11353–11363.
Alvarez, J.M., Rivas, H.J., Rossen, W.R., 2001. Unified model for steady-state foam behavior at high and low foam qualities. SPE J. 6 (03), 325–333.
Aronson, A.S., Bergeron, V., Fagan, M.E., Radke, C.J., 1994. The influence of disjoining pressure on foam stability and flow in porous media. Colloids Surf. A 83 (2), 109–120.
Aziz, K., Settari, A., 1979. Petroleum Reservoir Simulation. Chapman & Hall.
Bergeron, V., Fagan, M.E., Radke, C.J., 1993. Generalized entering coefficients: a criterion for foam stability against oil in porous media. Langmuir 9 (7), 1704–1713.
Chambers, K.T., Radke, C.J., 1991. Capillary phenomena in foam flow through porous media. Interfacial Phenom. Petr. Recovery 36, 191.
Chen, M., Yortsos, Y.C., Rossen, W.R., 2006. Pore-network study of the mechanisms of foam generation in porous media. Phys Rev E 73 (3), 036304.
Chen, Q., 2009. Assessing and improving steam-assisted gravity drainage: reservoir heterogeneities, hydraulic fractures, and mobility control foams. Stanford University Ph.D. thesis.
Chen, Q., Gerritsen, M., Kovscek, A.R., 2010. Modeling foam displacement with the local-equilibrium approximation: theory and experimental verification. SPE J. 15 (01), 171–183.
Cohen, D., Patzek, T.W., Radke, C.J., 1997. Onset of mobilization and the fraction of trapped foam in porous media. Transp. Porous Media 28 (3), 253–284.
Eide, Ø., Fernø, M., Bryant, S., Kovscek, A., Gauteplass, J., 2020. Population-balance modeling of CO2 foam for CCUS using nanoparticles. J. Nat. Gas Sci. Eng. 103378.
Ettinger, R.A., Radke, C.J., 1992. The influence of texture on steady foam flow in Berea sandstone. SPE Reservoir Eng. 7 (01).
Falls, A.H., Hirasaki, G.J., Patzek, T.W., Gauglitz, D.A., Miller, D.D., Ratulowski, T., 1988. Development of a mechanistic foam simulator: the population balance and generation by snap-off. SPE Reservoir Eng. 3 (03), 884–892.
Falls, A.H., Musters, J.J., Ratulowski, J., 1989. The apparent viscosity of foams in homogeneous bead packs. SPE Reservoir Eng. 4 (02), 155–164.
Farajzadeh, R., Andrianov, A., Krastev, R., Hirasaki, G.J., Rossen, W., 2012. Foam–oil interaction in porous media: implications for foam assisted enhanced oil recovery. Adv. Colloid Interface Sci. 183, 1–13.
Friedmann, F., Chen, W.H., Gauglitz, P.A., 1991. Experimental and simulation study of high-temperature foam displacement in porous media. SPE Reservoir Eng. 6 (01), 37–45.
Friedmann, F., Jensen, J.A., 1986. Some parameters influencing the formation and propagation of foams in porous media. SPE California Regional Meeting. Society of Petroleum Engineers.
Gillis, J.V., Radke, C.J., 1990. A dual gas tracer technique for determining trapped gas saturation during steady foam flow in porous media. In: SPE Annual Technical Conference and Exhibition. Society of Petroleum Engineers.
Hirasaki, G.J., Lawson, J.B., 1985. Mechanisms of foam flow in porous media: apparent viscosity in smooth capillaries. SPE J. 25 (2), 176–190.
Hirasaki, G.J., Miller, C.A., Szafranski, R., Lawson, J.B., Akiya, N., 1997. Surfactant/foam process for aquifer remediation. International Symposium on Oilfield Chemistry. Society of Petroleum Engineers.
Hirasaki, G.J., Miller, C.A., Szafranski, R., Tanzil, D., Lawson, J.B., Meinardus, H., Jin, M., Londergan, J.T., Jackson, R.E., Pope, G.A., Wade, W.H., 1997. Field demonstration of the surfactant/foam process for aquifer remediation. In: SPE Annual Technical Conference and Exhibition. Society of Petroleum Engineers.
Jimenez, A.I., Radke, C.J., 1989. Dynamic stability of foam lamellae flowing through a periodically constricted pore, pp. 460–479. Chapter 26
Kahrobaei, S., Farajzadeh, R., 2019. Insights into effects of surfactant concentration on foam behavior in porous media. Energy Fuels 33 (2), 822–829.
Kharabaf, H., Yortsos, Y.C., 1997. Invasion percolation with memory. Phys Rev E 55 (6), 7177.
Kharabaf, H., Yortsos, Y.C., 1998. A pore-network model for foam formation and propagation in porous media. SPE J. 3 (01), 42–53.

Khatib, Z.I., Hirasaki, G.J., Falls, A.H., 1988. Effects of capillary pressure on coalescence and phase mobilities in foams flowing through porous media. SPE Reservoir Eng. 3 (03), 919–926.

Kovscek, A.R., Patzek, T.W., Radke, C.J., 1995. A mechanistic population balance model for transient and steady-state foam flow in boise sandstone. Chem. Eng. Sci. 50 (23), 3783–3799.

Kovscek, A.R., Radke, C.J., 1994. Fundamentals of foam transport in porous media. ACS Adv. Chem. Ser. 242, 115–164.

Kovscek, A.R., Radke, C.J., 1996. Gas bubble snap-off under pressure-driven flow in constricted noncircular capillaries. Colloids and Surf. A 117 (1), 55–76.

Li, B., Hirasaki, G.J., Miller, C.A., 2006. Upscaling of foam mobility control to three dimensions. SPE/DOE Symposium on Improved Oil Recovery. Society of Petroleum Engineers.

Liontas, R., Ma, K., Hirasaki, G.J., Biswal, S.L., 2013. Neighbor-induced bubble pinch-off: novel mechanisms of in situ foam generation in microfluidic channels. Soft Matter 9 (46), 10971–10984.

Ma, K., Mateen, K., Ren, G., Luo, H., Neillo, V., Blondeau, C., Bourdarot, G., Morel, D., M'barki, O., Nguyen, Q., 2019. Parameter estimation of a population-balance foam model using two-step multi-variable search. In: IOR 2019–20th European Symposium on Improved Oil Recovery, Vol. 2019. European Association of Geoscientists & Engineers, pp. 1–21.

Ma, K., Ren, G., Mateen, K., Morel, D., Cordelier, P., 2015. Modeling techniques for foam flow in porous media. SPE J. 20 (03), 453–470.

Mamun, C.K., Rong, J.G., Kam, S.I., Liljestrand, H.M., Rossen, W.R., 2002. Extending foam technology from improved oil recovery to environmental remediation. In: SPE Annual Technical Conference and Exhibition. Society of Petroleum Engineers.

Manlowe, D.J., Radke, C.J., 1990. A pore-level investigation of foam/oil interactions in porous media. SPE Reservoir Eng. 5 (04), 495–502.

Myers, T.J., 1999. The role of residual oil in the mechanistic simulation of foam flow in porous media: experiment and simulation with the population-balance method. Ph.D. thesis.

Myers, T.J., Radke, C.J., 2000. Transient foam displacement in the presence of residual oil: experiment and simulation using a population-balance model. Ind. Eng. Chem. Res. 39 (8), 2725–2741.

Nguyen, Q.P., Rossen, W.R., Zitha, P.L.J., Currie, P.K., 2009. Determination of gas trapping with foam using x-ray computed tomography and effluent analysis. SPE J. 14 (02), 222–236.

Oolman, T., Godard, S.T., Pope, G.A., Jin, M., Kirchner, K., 1995. DNAPL flow behavior in a contaminated aquifer: evaluation of field data. Groundwater Monit. Rem. 15 (4), 125–137.

Osterloh, W.T., Jante, M.J., 1992. Effects of gas and liquid velocity on steady-state foam flow at high temperature. SPE/DOE Enhanced Oil Recovery Symposium. Society of Petroleum Engineers.

Pancharoen, M., Fernø, M.A., Kovscek, A.R., 2012. Modeling foam displacement in fractures. J. Pet. Sci. Eng. 100, 50–58.

Patzek, T.W., 1988. Description of Foam Flow in Porous Media by the Population Balance Method. American Chemical Society, Washington, DC, pp. 326–341. chapter 17

Persoff, P., Radke, C., Pruess, K., Benson, S., Witherspoon, P., 1989. A laboratory investigation of foam flow in sandstone at elevated pressure. SPE California Regional Meeting. Society of Petroleum Engineers.

Pope, G.A., Wade, W.H., 1995. Lessons from Enhanced Oil Recovery Research for Surfactant-Enhanced Aquifer Remediation. ACS Publications.

Ransohoff, T.C., Radke, C.J., 1988. Mechanisms of foam generation in glass-bead packs. SPE Reservoir Eng. 3 (02), 573–585.

Rin, R., Tomin, P., Garipov, T., Voskov, D., Tchelepi, H., 2017. General implicit coupling framework for multi-physics problems. In: SPE Reservoir Simulation Conference. Society of Petroleum Engineers.

Schramm, L.L., Novosad, J.J., 1990. Micro-visualization of foam interactions with a crude oil. Colloids Surf. 46 (1), 21–43.

Szafranski, R., Lawson, J.B., Hirasaki, G.J., Miller, C.A., Akiya, N., King, S., Jackson, R.E., Meinardus, H., Londergan, J., 1998. Surfactant/foam process for improved efficiency of aquifer remediation. In: Structure, Dynamics and Properties of Disperse Colloidal Systems. Springer, pp. 162–167.

Tang, G.-Q., Kovscek, A.R., 2006. Trapped gas fraction during steady-state foam flow. Transp. Porous Media 65 (2), 287–307.

Voskov, D., Tchelepi, H., 2012. Comparison of nonlinear formulations for two-phase multi-component EoS based simulation. J. Pet. Sci. Eng. 82, 101–111.

Wang, S., Mulligan, C.N., 2004. An evaluation of surfactant foam technology in remediation of contaminated soil. Chemosphere 57 (9), 1079–1089.

Wong, Z.Y., Horne, R.N., Tchelepi, H.A., 2018. Sequential implicit nonlinear solver for geothermal simulation. J. Comput. Phys. 368, 236–253.

Wong, Z.Y., Kwok, F., Horne, R.N., Tchelepi, H.A., 2019. Sequential-implicit newton method for multiphysics simulation. J. Comput. Phys..

Zhou, Y., 2012. Parallel general-purpose reservoir simulation with coupled reservoir models and multisegment wells. Stanford University Ph.D. thesis.

Zhou, Y., Tchelepi, H., Mallison, B., 2011. Automatic differentiation framework for compositional simulation on unstructured grids with multi-point discretization schemes. SPE Reservoir Simulation Symposium. Society of Petroleum Engineers.